Supporting Information

for

An Electron Acceptor with Intrinsic Quinoidal Core for Bulk-Heterojunction Organic Solar Cells and Photodetectors

Haozhe Feng,‡[a] Bingyan Yin,‡[a] Langheng Pan, ‡[a] Xinyuan Liu,‡[a] Seoyoung Kim,[b] Yanfei Zhao,*[c] Xuelong Huang*[d] Changduk Yang,[b] Chunhui Duan*[a]

‡ These authors contributed equally to this work.

[a] *Institute of Polymer Optoelectronic Materials and Devices*, *State Key Laboratory of Luminescent Materials and Devices*, *South China University of Technology*, *Guangzhou 510640*, *China*.

[b] *School of Energy and Chemical Engineering, Perovtronics Research Center, Low Dimensional Carbon Materials Center, Ulsan National Institute of Science and Technology (UNIST), 50 UNIST-gil, Ulju-gun, Ulsan 44919, South Korea.*

[c] *School of Materials Science and Engineering, Dongguan University of Technology, Dongguan 523808, P. R. China.*

[d] *Key Laboratory of Prevention and Treatment of Cardiovascular and Cerebrovascular Diseases of Ministry of Education, Gannan Medical University, Ganzhou 341000, People's Republic of China.*

E-mail: duanchunhui@scut.edu.cn; yanfei_zhao0923@163.com; huangxuelong@gmu.edu.cn

1. Synthesis

The starting chemical (compound 1) was synthesized according to the method reported in literatures.[1-3] Other chemicals and solvents were purchased from commercial sources (Sigma-Aldrich, Acros, Stream, or Alfa Aesar) and used directly unless otherwise noted.

Synthesis of compound 2: In a 100 mL two-necked flask, compound 1 (500 mg, 1.004 mmol) and K_2CO_3 (415 mg, 3.0 mmol) were dissolved in anhydrous *N*,*N*-dimethylformamide (DMF) (50 mL) and then 7-(bromomethyl)pentadecane (0.98 g, 3.2 mmol) was added in portions to the reaction mixture. The resulting mixture was stirred and heated at 130 °C overnight. The mixture was then cooled to room temperature, poured into water (80 mL), and stirred for 5 minutes. The product was extracted with dichloromethane, washed with water, and dried over anhydrous $MgSO_4$ to obtain crude product. The crude product was purified by silica gel chromatography using a solvent mixture of dichloromethane/petroleum ether (1/1, v/v) as eluent to obtain compound 2 as a dark red solid (602 mg, 63% yield). ^{1}H NMR (500 MHz, $CDCl_3$) δ: 8.37 (d, J = 8.7 Hz, 4H), 7.57 (d, J = 8.7 Hz, 4H), 3.64 (d, J = 7.2 Hz, 4H), 1.99-1.90 (m, 2H), 1.27 (m, 48H), 0.86 (t, J = 6.9 Hz, 12H). ^{13}C NMR (125 MHz, $CDCl_3$) δ: 170.23, 160.28, 136.06, 131.72, 131.33, 128.92, 124.58, 120.49, 42.74, 36.97, 31.80, 31.78, 31.58, 31.56, 29.94, 29.62, 29.52, 29.24, 26.39, 26.38, 22.57, 14.02, 14.01. MS (MALDI-TOF) Calcd. For $C_{52}H_{74}Br_2N_4O_2$: 947.00, found: 946.36. Elemental analysis Calcd, N: 5.92 %, C: 65.95%, H: 7.88%, S: 0%; Found, N: 5.76%, C: 65.33%, H: 7.72%, S: 0%. Melting point: 134–143°C.

Synthesis of compound 3: Compound 2 (500 mg, 0.53 mmol) and (4,4-bis(2-ethylhexyl)-4H-cyclopenta[2,1-b:3,4-b']dithiophen-2-yl)tributylstannane (1.1 g, 1.59 mmol) were dissolved in anhydrous *o*-xylene (30 mL) in a two-necked flask. The mixture was degassed with nitrogen for 15 minutes. $Pd_2(dba)_3$ (24 mg, 0.026 mmol) and P(*o*-tol)$_3$ ligand (64 mg, 0.21 mmol) were added, and the resulting mixture was heated to 140 °C and stirred overnight. The mixture was then poured into brine and extracted three times with dichloromethane. After removal of the solvent, the product was purified by silica gel column chromatography using a solvent mixture of dichloromethane/petroleum ether (1/3, v/v) as eluent to obtain compound 3 as an orange-red oil (604 mg, 72% yield). ^{1}H NMR (500 MHz, $CDCl_3$) δ: 8.60 (d, J = 8.8 Hz, 4H), 7.66 (d, J = 8.7 Hz, 4H), 7.31 (d, J = 1.3 Hz, 2H), 7.19 (d, J = 4.8 Hz, 2H), 6.96 (m, 2H), 3.69 (d, J = 7.2 Hz, 4H), 2.07-1.85 (m, 10H), 1.51-1.19 (m, 48H), 1.08-0.82 (m, 42H), 0.80-0.54 (m, 30H). ^{13}C NMR (125 MHz, $CDCl_3$) δ:

169.66, 158.60, 157.81, 156.99, 142.02, 137.03, 135.83, 135.48, 134.16, 129.57, 128.14, 124.22, 123.77, 121.36, 119.76, 118.22, 52.69, 42.25, 42.19, 41.73, 36.10, 34.10, 33.17, 33.12, 33.10, 30.91, 30.88, 30.79, 30.76, 29.09, 28.78, 28.68, 28.65, 28.38, 27.57, 26.36, 26.34, 26.31, 25.60, 21.74, 21.71, 21.68, 13.13, 13.11, 13.05, 9.69, 9.68, 9.58. MS(MALDI-TOF) Calcd. For $C_{102}H_{148}N_4O_2S_4$: 1590.57, found: 1590.10.

Synthesis of compound 4: To a solution of compound 3 (500 mg, 0.31 mmol) in 1,2-dichloroethane (10 mL) and *N*,*N*-dimethylformamide (DMF) (5 mL) at 0 °C, phosphorus oxychloride (0.4 mL, 4.7 mmol) was added dropwise under nitrogen protection. The mixture was stirred at 0 °C for 1 hour, then refluxed overnight. The reaction mixture was poured into water (150 mL) and extracted three times with chloroform. The combined organic layers were washed with water, dried over Na_2SO_4, and the solvent was evaporated under reduced pressure. The residue was purified by column chromatography on silica gel, eluting with a mixture of petroleum ether/dichloromethane (1:1, v/v) to afford compound 4 as an orange oil (397 mg, 78% yield). ^{1}H NMR (500 MHz, $CDCl_3$) δ: 9.85 (s, 2H), 8.62 (d, J = 8.7 Hz, 4H), 7.69 (d, J = 8.7 Hz, 4H), 7.58 (s, 2H), 7.34 (s, 2H), 3.70 (d, J = 7.1 Hz, 4H), 2.07-1.89 (m, 10H), 1.58-1.16 (m, 48H), 1.11-0.81 (m, 42H), 0.80-0.47 (m, 30H). ^{13}C NMR (125 MHz, $CDCl_3$) δ: 182.50, 170.55, 163.05, 159.99, 157.77, 148.05, 147.67, 143.48, 136.43, 135.75, 135.54, 130.71, 130.13, 125.33, 120.66, 119.13, 119.03, 54.21, 43.15, 42.81, 37.14, 35.31, 35.29, 34.30, 34.28, 34.12, 31.94, 31.90, 31.79, 31.76, 30.09, 29.80, 29.66, 29.38, 28.57, 28.55, 27.51, 27.49, 27.31, 26.60, 22.74, 22.69, 14.16, 14.14, 14.06, 14.04, 10.69, 10.68, 10.58. MS(MALDI-TOF) Calcd. For $C_{104}H_{148}N_4O_4S_4$: 1646.59, found: 1645.99.

Synthesis of PzDP-IC2Cl: Compound 4 (280 mg, 0.17 mmol), 2-(5,6-dichloro-3-oxo-2,3-dihydro-1H-inden-1-ylidene) acetonitrile (227 mg, 0.86 mmol), and anhydrous chloroform (40 mL) were added to a 100 mL two-necked flask. The mixture was degassed with nitrogen for 15 minutes, and then 0.6 mL of pyridine was added. The mixture was stirred at 65 °C for 6 hours. After cooling to room temperature, the mixture was poured into 100 mL of methanol and the precipitate was collected by filtration. The precipitate was then redissolved in chloroform and reprecipitated from methanol. This dissolution-precipitation process was repeated three times, and the final product was purified by silica gel and gel filtration columns. The purified product was then crystallized from chloroform/methanol to give PzDP-IC2Cl as a brownish-yellow solid (310 mg, 84% yield). ^{1}H NMR (500 MHz, $CDCl_3$) δ: 8.91 (s, 2H), 8.71 (s, 2H), 8.62 (d, J = 8.3 Hz, 4H), 7.89 (s, 2H), 7.67-7.69 (m,

6H), 7.40 (s, 2H), 3.71 (d, *J* = 6.8 Hz, 4H), 2.13-1.89 (m, 10H), 1.65-1.13 (m, 48H), 1.13-0.82 (m, 42H), 0.71 (m, 30H). ^{13}C NMR(125 MHz, $CDCl_3$) *δ*: 186.13, 170.38, 166.94, 159.99, 159.61, 158.30, 152.58, 139.45, 139.21, 138.98, 138.64, 137.08, 136.03, 134.88, 131.04, 130.74, 126.77, 125.58, 124.83, 120.27, 119.34, 114.78, 114.67, 67.94, 54.16, 43.26, 43.17, 42.84, 37.17, 35.52, 35.48, 34.25, 34.04, 31.93, 31.91, 31.75, 30.08, 29.77, 29.65, 29.39, 28.49, 28.45, 27.47, 27.29, 26.57, 22.84, 22.81, 22.73, 22.70, 14.18, 14.14, 14.10, 14.06, 10.58. MS(MALDI-TOF) Calcd. For $C_{128}H_{152}Cl_4N_8O_4S_4$: 2136.72, found: 2136.94. Elemental analysis Calcd, N: 5.24 %, C: 71.95%, H: 7.17%, S: 6.00%; Found, N: 5.13%, C: 70.86%, H: 7.10%, S: 6.21%.

2.Measurements and characterization

Nuclear magnetic resonance (NMR): ^{1}H and ^{13}C NMR were measured on a Bruker AV-500 MHz spectrometer in $CDCl_3$ (25 °C). Chemical shifts *δ* were reported in ppm using $CDCl_3$ (7.26 ppm for ^{1}H NMR and 77.0 ppm for ^{13}C NMR) as an internal standard.

MALDI-TOF-MS: MALDI-TOF-MS was measured on Bruker Daltronik GmbH (autoflex II).

Elemental analysis: Elemental analysis was carried out with Vario EL cube (Germany Elementar). The burning temperature: 100-110 °C, the reaction temperature: 1800 °C. Measuring range: C: 0.001-35 mg, H: 0.001-3mg, N: 0.001-15mg, S: 0.001-2 mg.

Thermogravimetric analyses (TGA): TGA were carried out with NETZSCH TG 209 at a heating rate of 10 °C min^{-1} with a nitrogen flow rate of 20 mL min^{-1}.

Differential scanning calorimetry (DSC): DSC measurements were performed on a NETZSCH (DSC200F3) apparatus under a nitrogen atmosphere with a heating/cooling rate of 10/20 °C min^{-1} for the first cycle and a heating/cooling rate of 10/20 °C min^{-1} for the second cycle, respectively.

UV-vis-NIR absorption spectra: UV-vis-NIR spectra were recorded on a Shimadzu UV-3600 spectrophotometer. The solutions were prepared in chloroform with the concentration of 0.02 mg mL^{-1}. The films were prepared by spin coating the chloroform solutions onto glass substrates.

Cyclic voltammetry (CV): Cyclic voltammetry measurements were conducted on a CHI660A electrochemical workstation in a solution of tetrabutylammonium hexafluorophosphate (Bu4NPF6, 0.1 mol L^{-1}) in acetonitrile. A glassy carbon, a platinum wire, and an Ag/AgCl electrode were used as working electrode, counter electrode, and reference electrode, respectively. A ferrocene/ferrocenium (Fc/Fc^+) redox couple was used as internal standard and was assigned an

absolute energy of –4.8 eV versus vacuum. The HOMO and LUMO energies of materials were determined according to the equation $E_{HOMO} = -(E_{ox\ onset} + 4.8 - E_{Fc/Fc+})$ and $E_{LUMO} = -(E_{red\ onset} + 4.8 - E_{Fc/Fc+})$, where $E_{ox\ onset}$ and $E_{red\ onset}$ are the onsets of oxidation and reduction potential. The formal potential of Fc/Fc+ redox couple was found at 0.44 V relative to the Ag/Ag^{+} electrode.

Density functional theory (DFT) calculation: The geometry and wave function distribution were fully optimized at the B3LYP/ 6-31+G* level of theory by the absence of imaginary frequencies. The long alkyl side chains were replaced by methyl groups. All calculations were carried out with the Gaussian 09 software.[4]

Photoluminescence (PL) quenching experiments: Emission spectra were recorded on an Edinburgh Instruments FLSP920 double-monochromator spectrophotometer and Shimadzu RF-6000 spectrometer.

Transmission electron microscope (TEM): TEM images were obtained from a JEM-2100F transmission electron microscope operated at 200 kV.

Grazing incidence wide-angle X-ray scattering (GIWAXS): The GIWAXS characterization for thin films was performed at PLS-II 9A USAXS beam line, Korea. X-rays coming from the in-vacuum undulator (IVU) were monochromated (wavelength λ≈1.11Å) in use of a double crystal monochromator with being focused both horizontally and vertically (450 (H) × 60 (V) μm^2 in FWHM at the sample position) by using K-B type mirrors. The scattering patterns were recorded by a 2D CCD detector (Rayonix SX165) with an irradiation time of 6-9 seconds, dependent on the saturation level of the detector. Diffraction angles were calibrated by using a sucrose standard (monoclinic, P21, a = 10.8631 Å, b = 8.7044 Å, c=7.7624 Å, β=102.938 Å and the sample-to-detector distance is ~230 mm.

3. Device fabrication and characterization

Fabrication of solar cells: The substrates with indium tin oxide (ITO) were cleaned by detergent, sonicated in deionized water, and isopropanol sequentially. After that, the clean substrates were dried in oven at 70°C. The substrates were subjected to plasma treatment at room temperature for 5 minutes. Then PEDOT:PSS (CLEVIOS™ PVP AI 4083 from Heraeus) was spin-coated on the ITO glass substrates at 3000 rpm for 30 seconds, followed by drying at 150 °C for 10 minutes. The substrates were transferred to a nitrogen-filled glove box. The active layers were spin-coated on

substrates at about 3000 rpm to give a thickness of 100 nm. Afterwards, a 10-nm thick PFN-Br was spin-coated from a methanol:ethanol=1:1 solution (0.5 mg mL^{-1}) at a spin speed of 2000 rpm for 30 seconds. Finally, a 100 nm Ag layer was thermally evaporated at a pressure of 5×10^{-6} Torr.

Fabrication of photodetectors: The OPDs with conventional device structure were fabricated the same as solar cells. The OPDs with inverted device structure were fabricated with the following procedures. The sol-gel zinc oxide (ZnO) was prepared by dissolving 0.3 g zinc acetate in 2.81 mL 2-methoxyethanol with 84.87 μL ethanolamine, and then stirred at 50 °C overnight. A 30 nm thick ZnO film was spun onto the ITO substrates and thermally annealed on a hot plate at 180 °C for 15 minutes. The substrates were transferred to a nitrogen-filled glove box. The active layers for both conventional and inverted OPDs were prepared exactly the same as those for the optimal OSCs by using BN as the solvent additive. After that, a 10 nm MoO_3 film and a 100 nm Ag layer were sequentially deposited by thermal evaporation under a vacuum of 5×10^{-6} Torr.

Photovoltaic performance measurements: The photovoltaic performances of the OSCs were measured under AM1.5G irradiation derived from a solar simulator (Enlitech, Taiwan). The current density-voltage (*J*-*V*) curves were recorded by a Keithley 2400 source meter. The light intensity was 100 mW cm^{-2} in the test, which was calibrated by a China General Certification Center-certified reference monocrystal silicon cell (Enlitech).

External quantum efficiencies (EQEs): The EQEs were measured on a commercial QE measurement system (QE-R3011, Enlitech). The light intensity was calibrated by a standard monocrystalline silicon photovoltaic cell at each wavelength.

Light-intensity dependence measurements: The light-intensity dependence measurements were performed with irradiation between 10–100 mW cm^{-2}, and calibrated by a standard single-crystal silicon solar cell (Enlitech). The *J*-*V* curves were recorded with a Keithley 2400 source meter.

Fabrication of single-carrier devices: The device structures of the electron-only and hole-only devices are ITO/ZnO (30 nm)/active layer (100 nm)/PFN-Br (10 nm)/Ag (100 nm) and ITO/PEDOT:PSS (30 nm)/active layer (100 nm)/MoO_x (10 nm)/Ag (100 nm), respectively. The dark current densities of the blends were measured by applying a voltage between 0 and ±4 V with a Keithley 2400 source meter.

Characterization of single-carrier devices: The data were analyzed according to Mott–Gurney law, which considers a Poor-Frenkel type dependence of mobility on electric fields, given by $J = \frac{9}{8}\varepsilon_r\varepsilon_0\mu_0 \frac{V^2}{d^3}\exp(0.89\gamma\sqrt{V/d})$, where ε_0 is the permittivity of free space, ε_r is the dielectric constant of the polymer which is assumed to be 3 for organic semiconductors, μ_0 is the zero-field mobility, V is the voltage drop across the device, d is the thickness of the active layer, and γ is a parameter that describes the strength of the field-dependence effect. The hole and electron mobilities were extracted with the fit parameters at an electric field (E) of 1.5×10^5 V cm^{-1} by the Murgatroyd equation $\mu = \mu_0\exp(\gamma\sqrt{E})$.

Dark currents density measurements: The dark current density-voltage (*J*-*V*) curves of OPDs were recorded with a Keithley 2450 source meter under dark conditions.

X-ray photoelectron spectroscopy (XPS): XPS measurements of the samples (ITO/PEDOT:PSS/active layer and ITO/ZnO/active layer) were performed on ESCALAB Xi+ (Thermo Fisher Scientific). The samples were sputtered with an Ar+ gun at 2 kV × 3.3 µA and etched from the air/active layer interface. The scanning area of the XPS depth profile was 2.5 mm × 2.5 mm, and the composition data were acquired from an area equal to a circle with a diameter of 0.5 mm.

4. Additional figures and tables

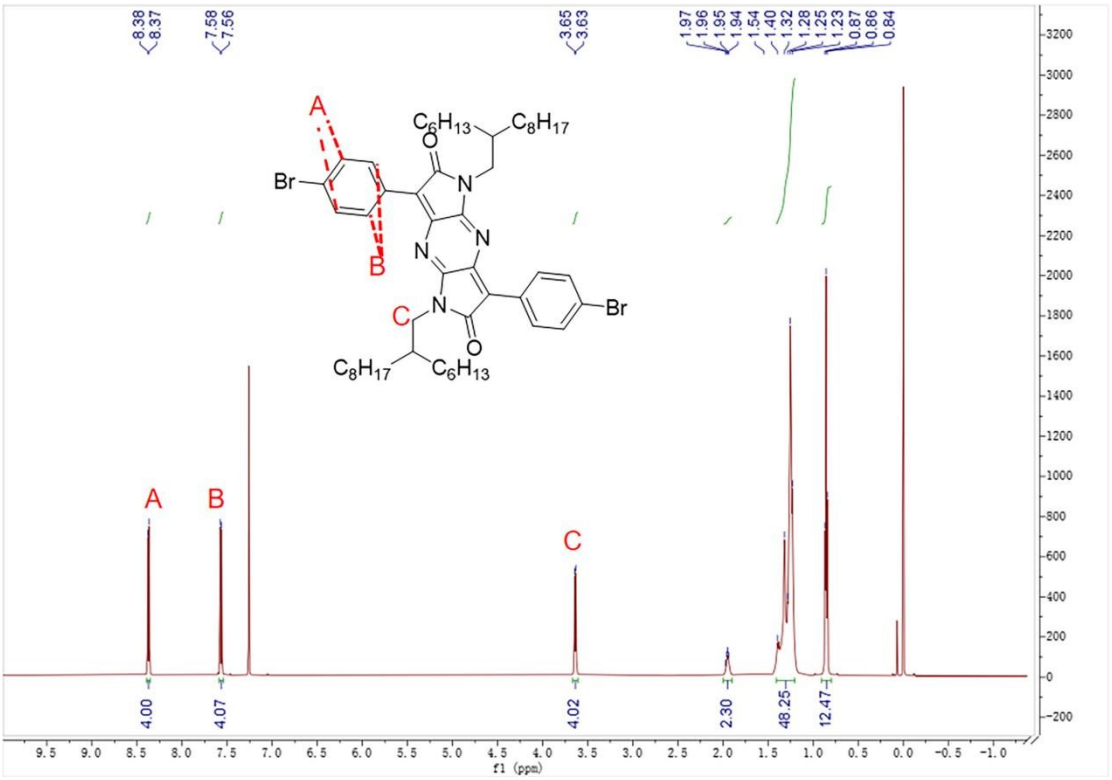

Fig. S1. ^{1}H NMR spectrum of the compound 2.

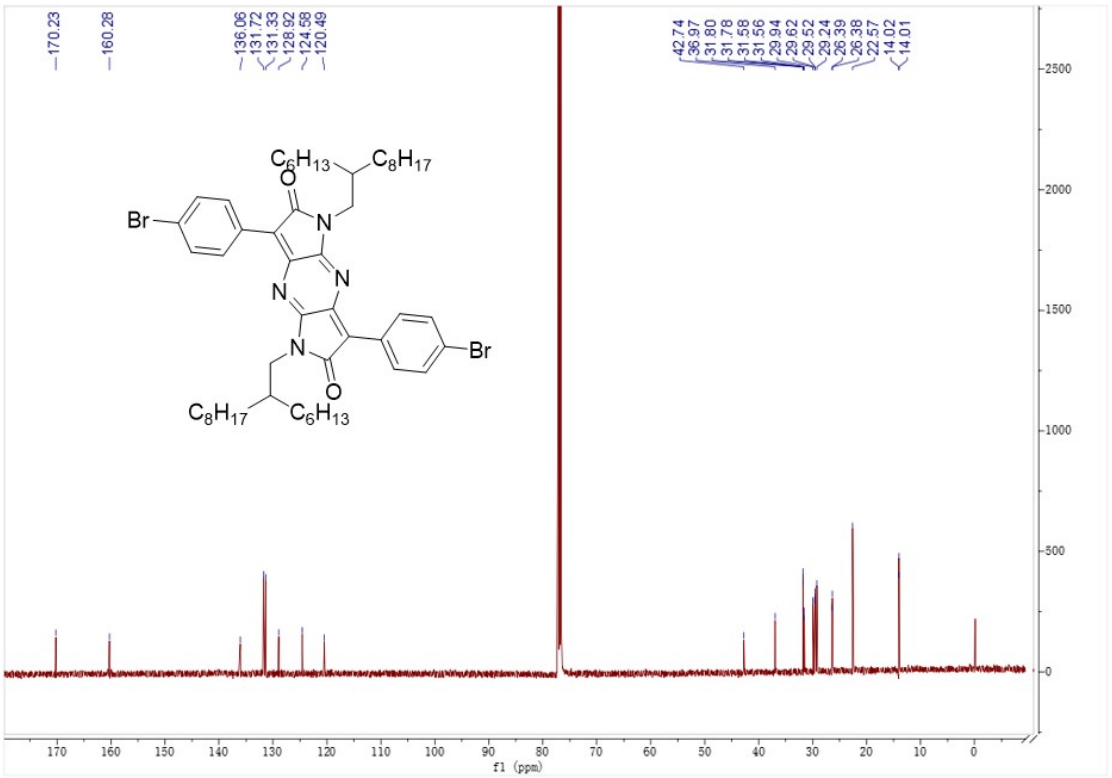

Fig. S2. ^{13}C NMR spectrum of the compound 2.

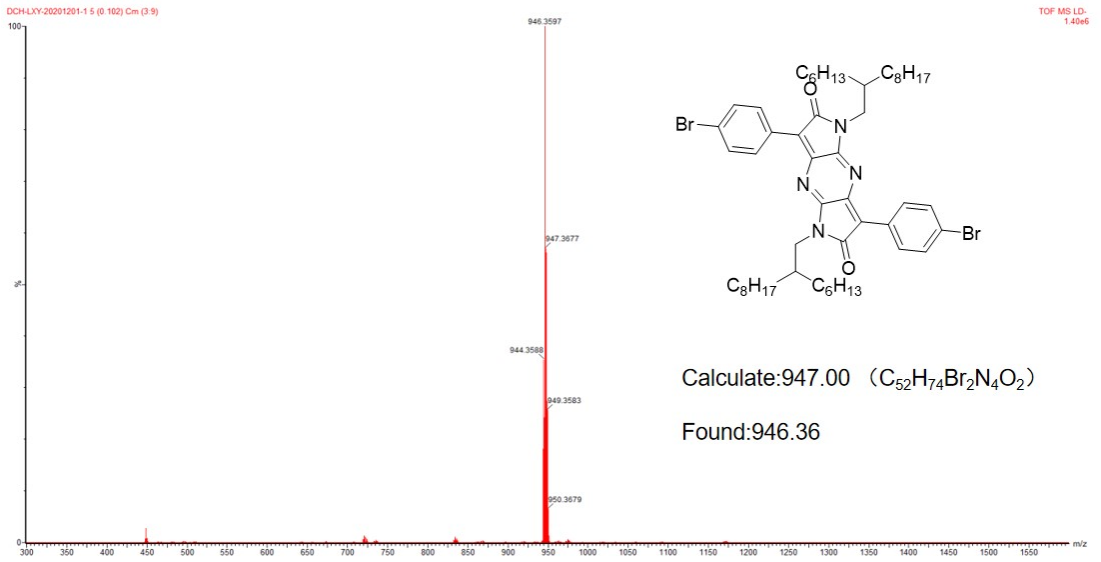

Fig. S3. MALDI-TOF of the compound 2.

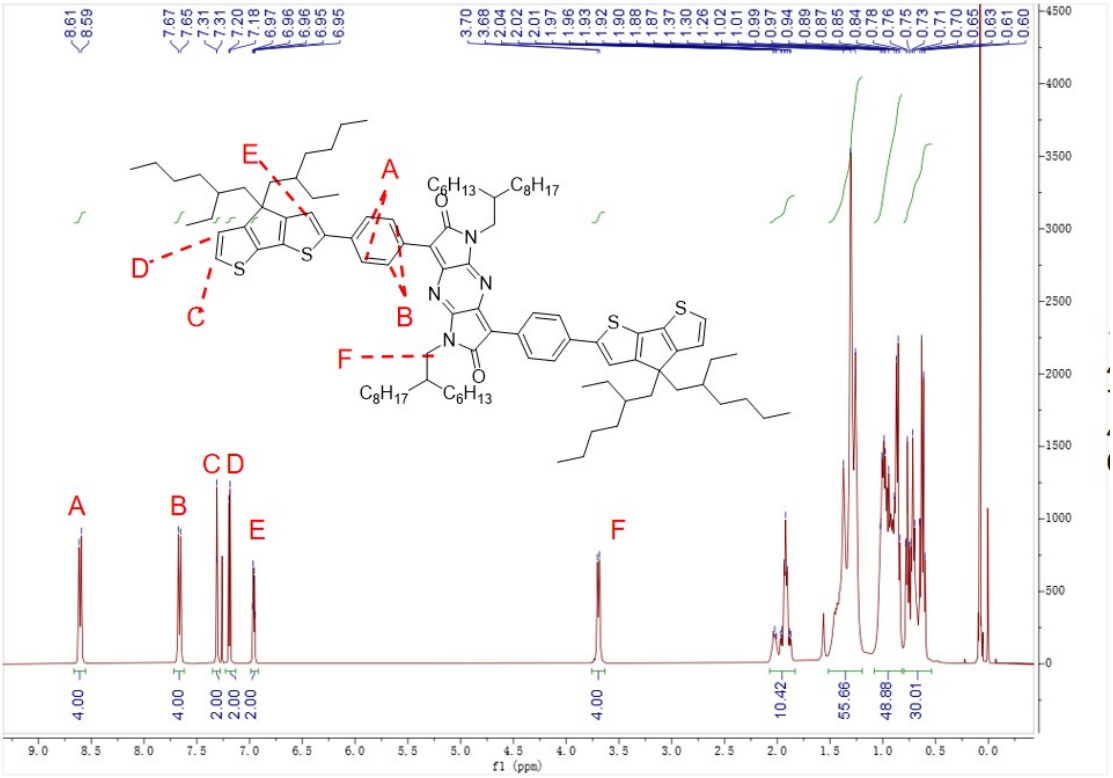

Fig. S4. ^{1}H NMR spectrum of the compound 3.

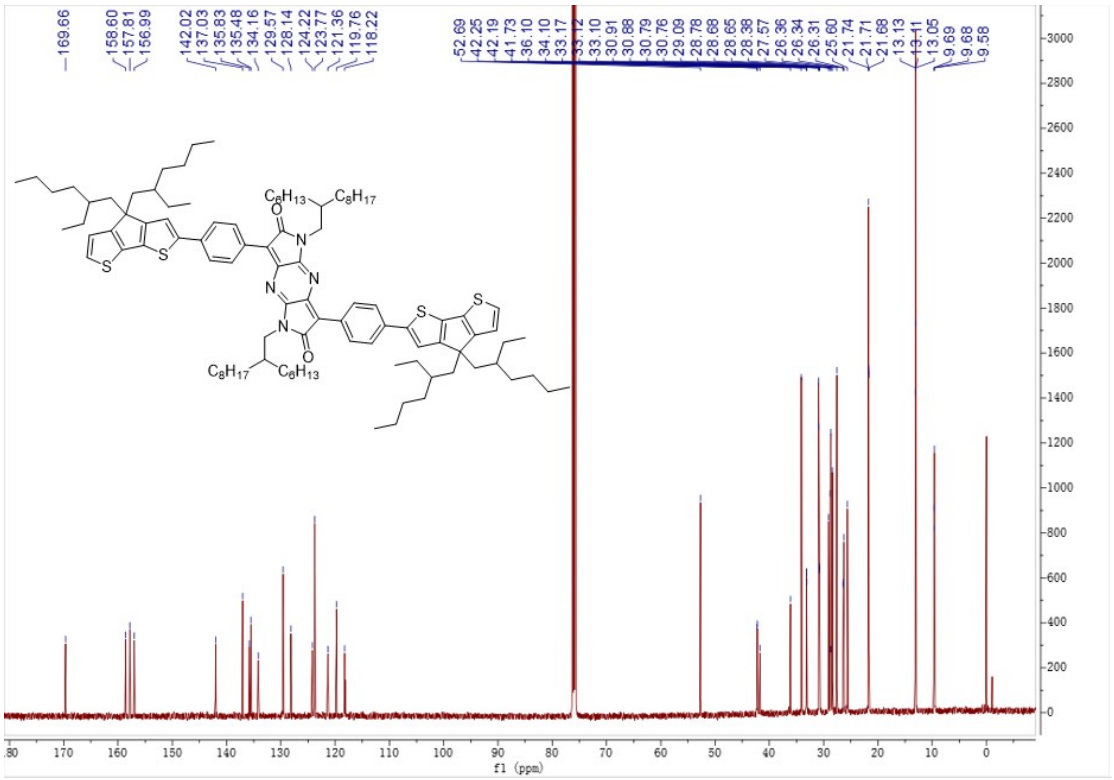

Fig. S5. ^{13}C NMR spectrum of the compound 3.

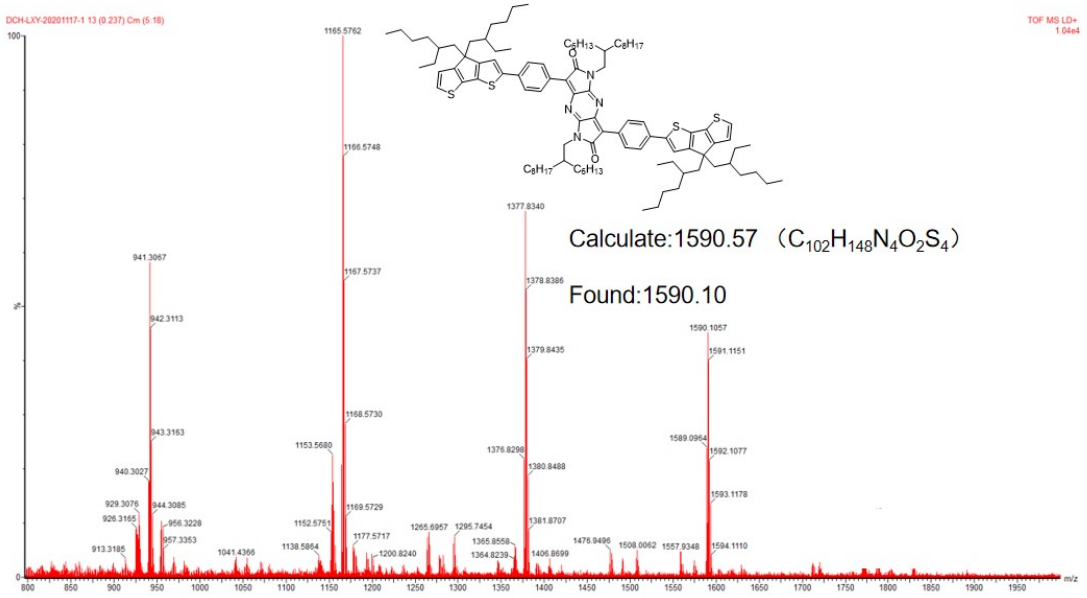

Fig. S6. MALDI-TOF of the compound 3.

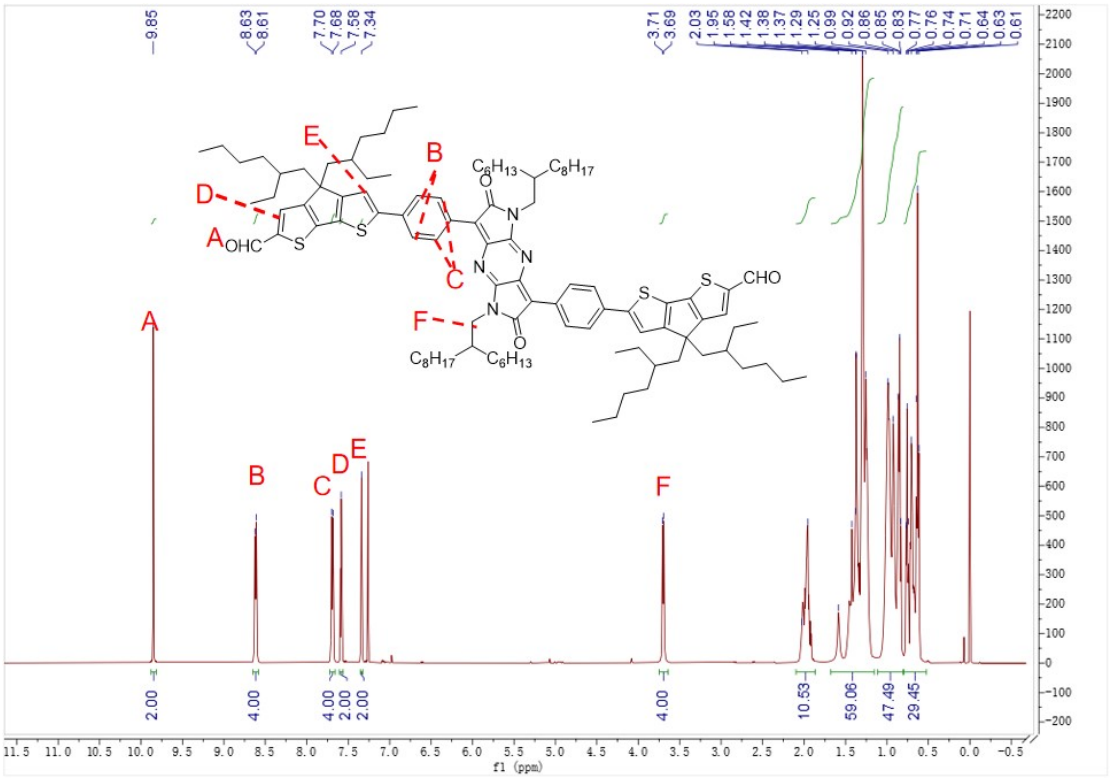

Fig. S7. ^{1}H NMR spectrum of the compound 4.

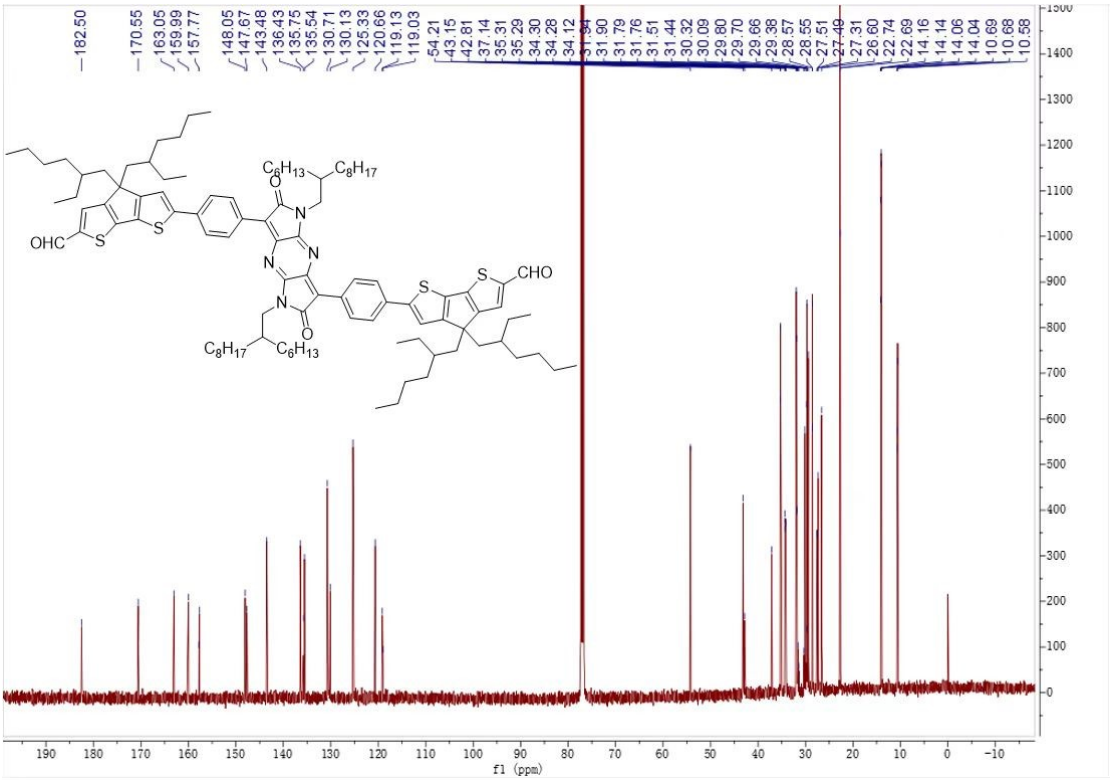

Fig. S8. ^{13}C NMR spectrum of the compound 4.

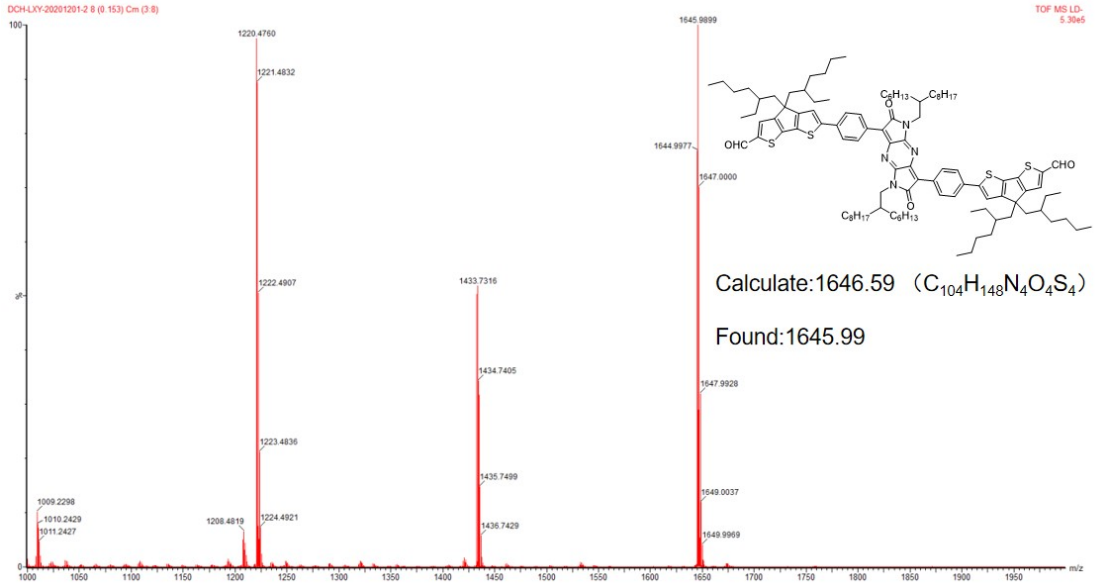

Fig. S9. MALDI-TOF of the compound 4.

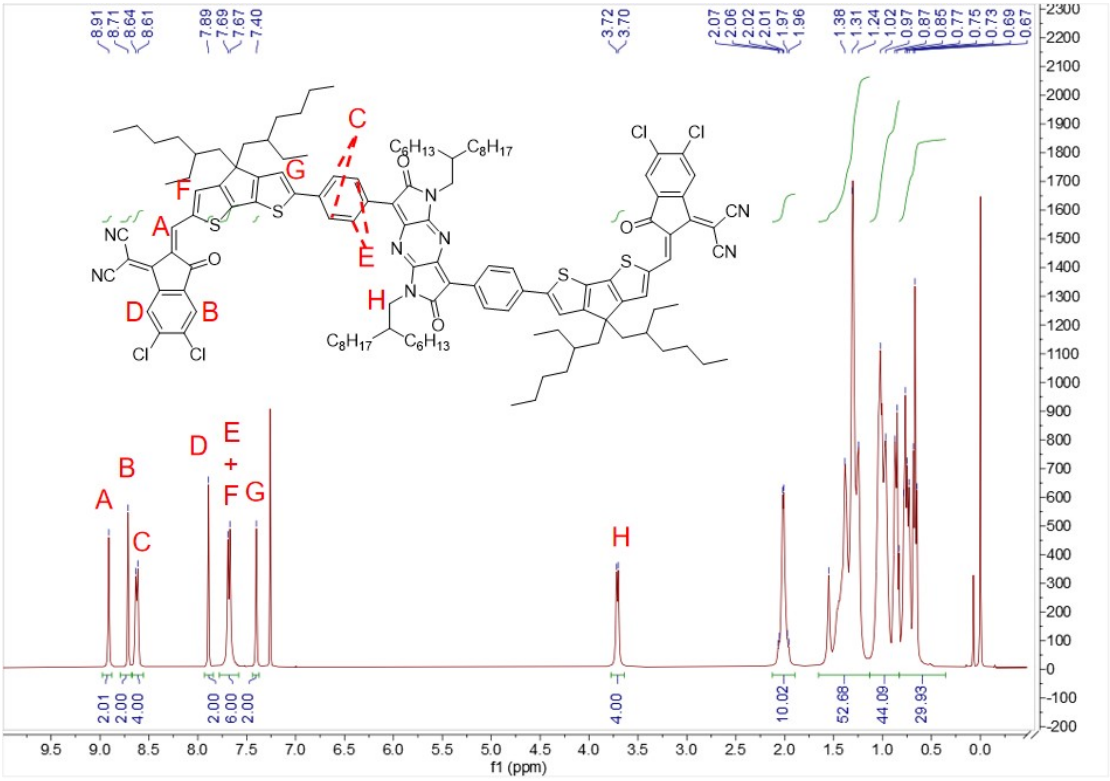

Fig. S10. ^{1}H NMR spectrum of PzDP-IC2Cl.

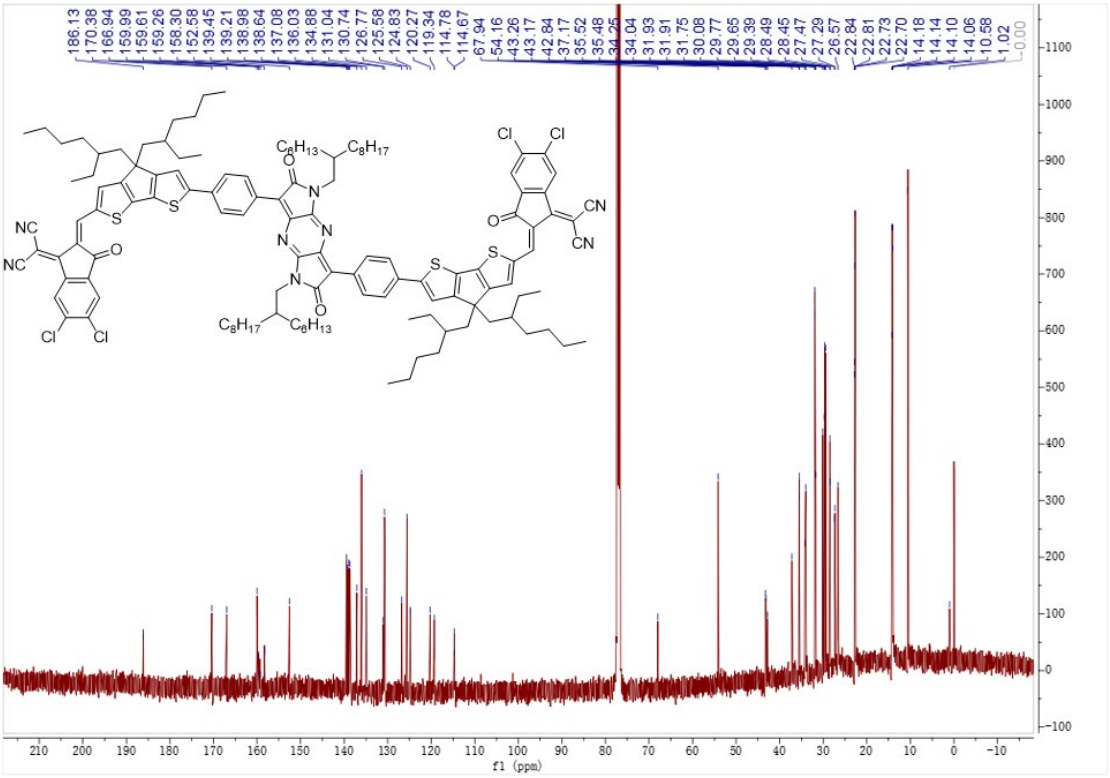

Fig. S11. ^{13}C NMR spectrum of PzDP-IC2Cl.

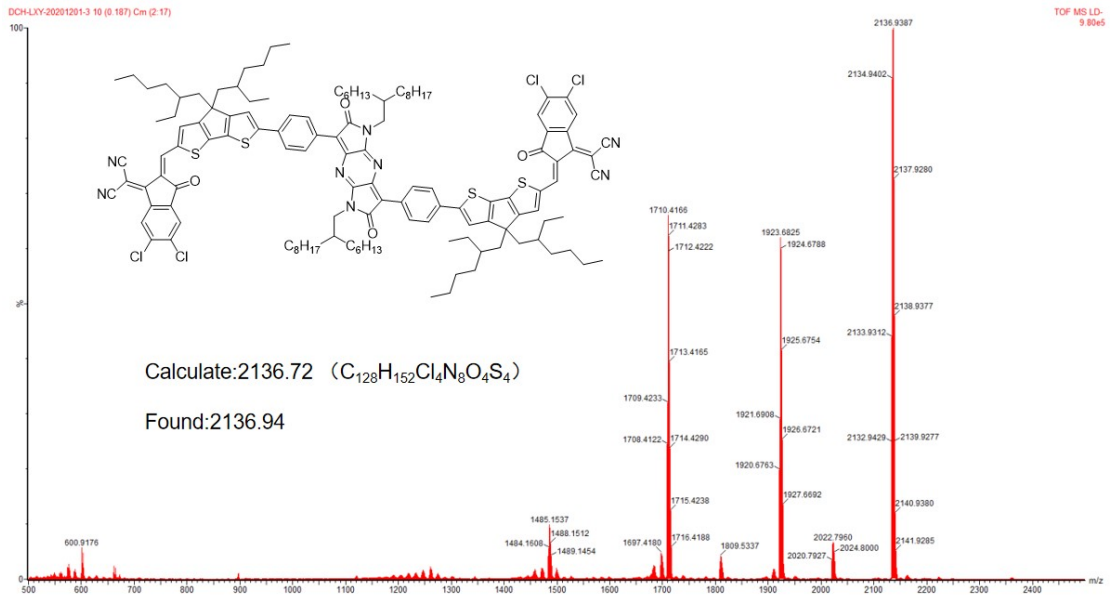

Fig. S12. MALDI-TOF of PzDP-IC2Cl.

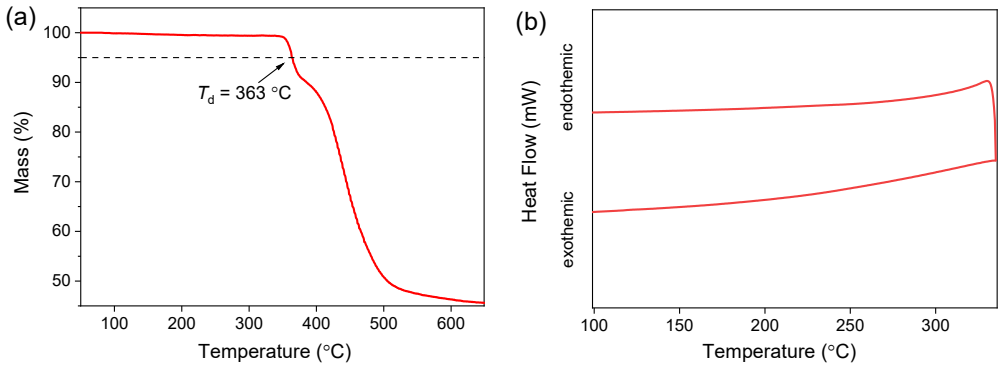

Fig. S13. (a) TGA plot of PzDP-IC2Cl with a heating rate of 10 °C min^{-1} under nitrogen atmosphere; (b) the second cycle of the DSC traces of PzDP-IC2Cl with a heating rate of 10 °C min^{-1} and cooling rate of 20 °C min^{-1}.

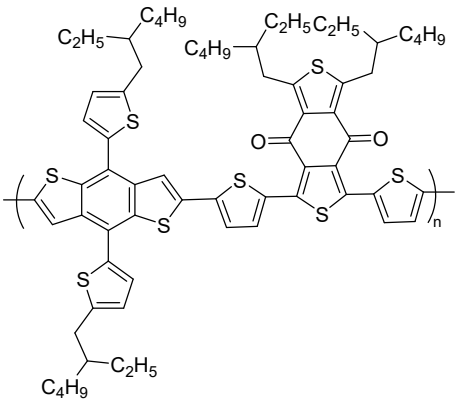

Fig. S14. The chemical structure of PBDB-T.

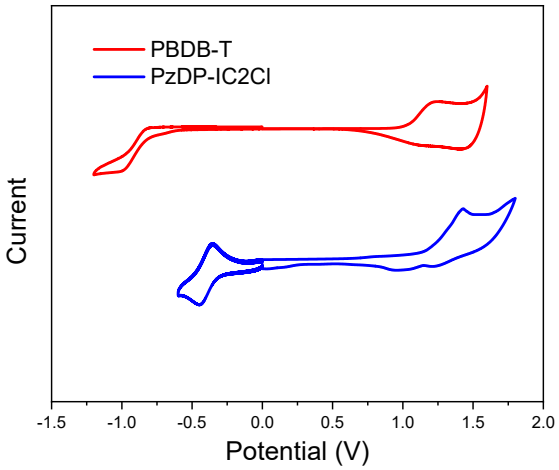

Fig. S15. Cyclic voltammetry curves of PBDB-T and PzDP-IC2Cl.

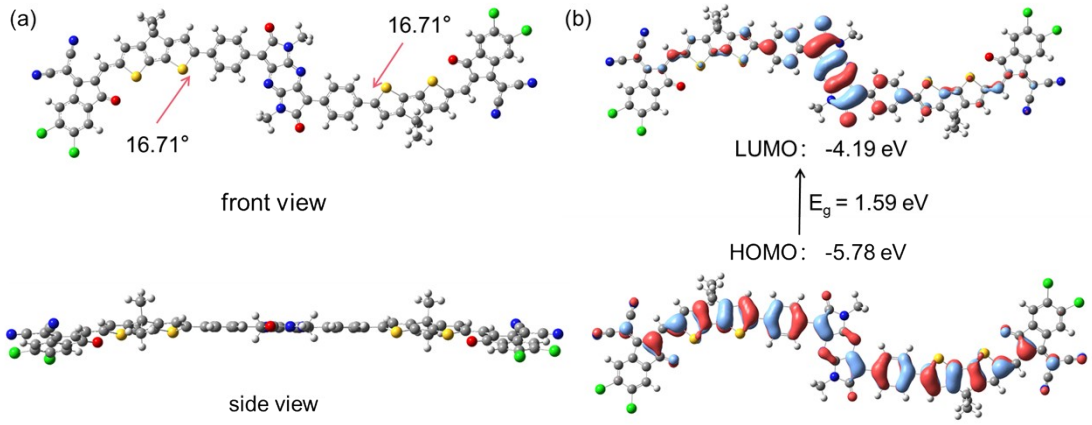

Fig. S16. (a) Front-view and side-view of optimized geometry and (b) wave function distribution of frontier molecular orbitals and energy levels of PzDP-IC2Cl simulated by DFT calculation. The long alkyl chains of PzDP-IC2Cl were replaced by methyl to simplify the calculations.

Table S1. Photovoltaic parameters of the OSCs based on PBDB-T:PzDP-IC2Cl blends under AM1.5G irradiation (100 mW cm^{-2}).

Solvent	D:A	TA	V_{oc} (V)	J_{sc} (mA cm^{-2})	FF (%)	PCE (%)
CF	1:1.2	w/o	0.670	11.05	46.99	3.45
CF	1:1	100 °C, 10 min	0.656	11.93	47.67	3.73
CF+0.5%DIO			0.633	15.32	55.06	5.37
CF+0.5%DPE			0.648	13.06	55.00	4.68
CF+0.5%CN			0.650	13.98	56.19	5.13
CF+0.5%BN			0.674	14.42	60.23	5.86
CF+0.5%NMP			0.649	12.26	50.79	4.06
CF+0.25%BN	1:1	100 °C, 10 min	0.645	14.34	49.16	4.55
CF+0.5%BN			0.677	14.62	59.45	5.88
CF+1%BN			0.680	12.30	54.89	4.59
CF+0.5%BN	1.2:1	w/o	0.692	13.51	59.05	5.53
	1:1		0.688	14.42	59.73	5.93
	1:1.2		0.689	14.80	63.10	6.43
	1:1.5		0.676	15.00	55.03	5.59
CF+0.5%BN	1:1.2	w/o	0.689	16.11	60.26	6.70
		80 °C, 10 min	0.686	14.32	60.39	5.94
		100 °C, 10 min	0.674	14.42	60.23	5.86
		120 °C, 10 min	0.674	13.96	60.12	5.67
		150 °C, 10 min	0.664	13.82	58.29	5.35

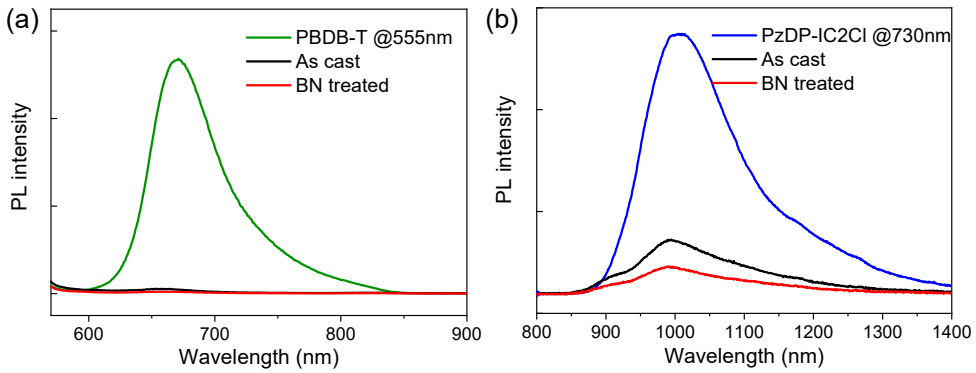

Fig. S17. The photoluminescence spectra of (a) PBDB-T and PBDB-T:PzDP-IC2Cl blend films excited at 555 nm, and (b) PzDP-IC2Cl and PBDB-T:PzDP-IC2Cl blend films excited at 730 nm.

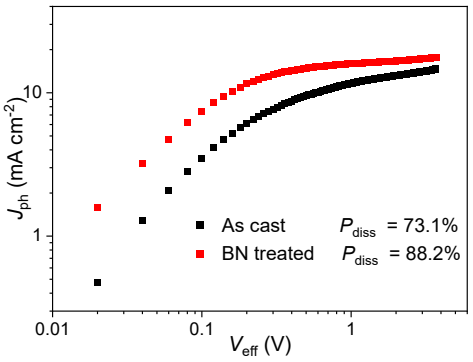

Fig. S18. The plots of J_{ph} versus V_{eff} of as cast and BN treated OSCs based on PzDP-IC2Cl.

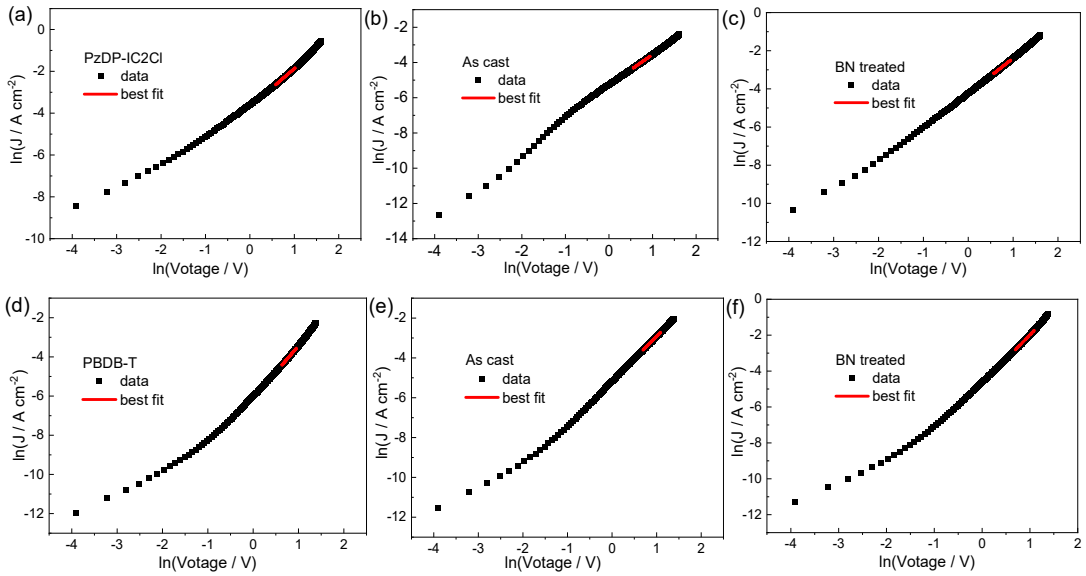

Fig. S19. (a-c) The *J*–*V* characteristics of the electron-only devices; (d-f) the *J*–*V* characteristics of the hole-only devices.

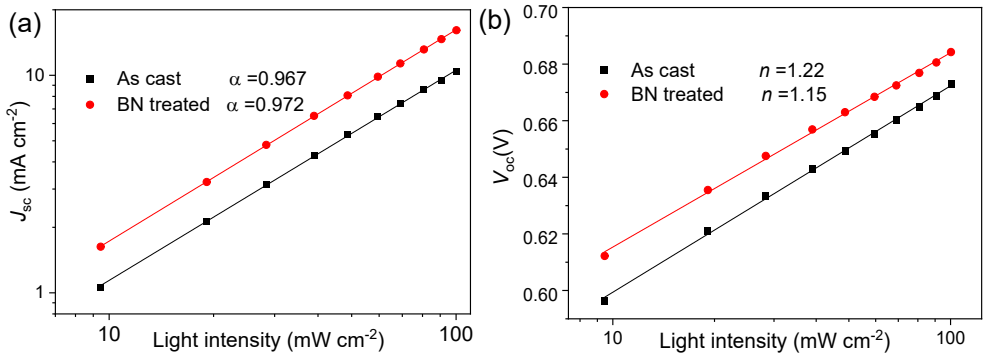

Fig. S20. (a) J_{sc} and (b) V_{oc} versus light intensity of the OSCs based on PBDB-T:PzDP-IC2Cl blends.

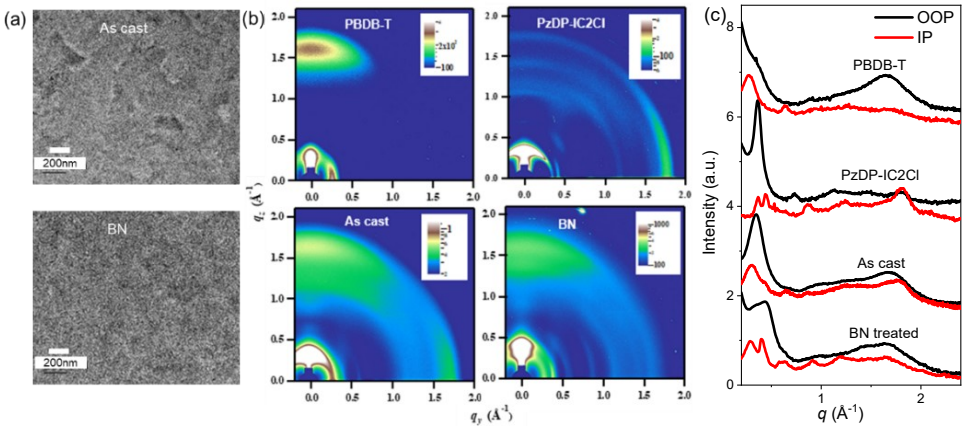

Fig. S21. (a) TEM images, (b) two-dimensional GIWAXS patterns, and (c) one-dimensional GIWAXS line-cut profiles of the corresponding films.

Table S2. GIWAXS parameters of the neat films.

Film	PBDB-T			PzDP-IC2Cl		
	q (Å^{-1})	*d*-spacing (Å)	CCL (Å)	*q* (Å^{-1})	*d*-spacing (Å)	CCL [a] (Å)
OOP (010)	1.63	3.85	17.6	-	-	-
IP (100)	0.28	22.4	63.6	0.37	17.0	175.5
OOP (100)	-	-	-	0.36	17.3	157.5
IP (010)	-	-	-	1.80	3.48	50.1

[a] CCL represents crystal coherence length.

Table S3. GIWAXS parameters of the blend films.

Film	As cast			BN treated		
	q (Å^{-1})	*d*-spacing (Å)	CCL (Å)	*q* (Å^{-1})	*d*-spacing (Å)	CCL (Å)
OOP (010)	1.66	3.78	18.7	1.62	3.87	14.9
IP (100)	0.30	20.9	51.0	0.29	21.7	68.3
OOP (100)	0.35	17.9	70.7	0.43	14.6	50.4
IP (010)	1.74	3.61	26.7	-	-	-

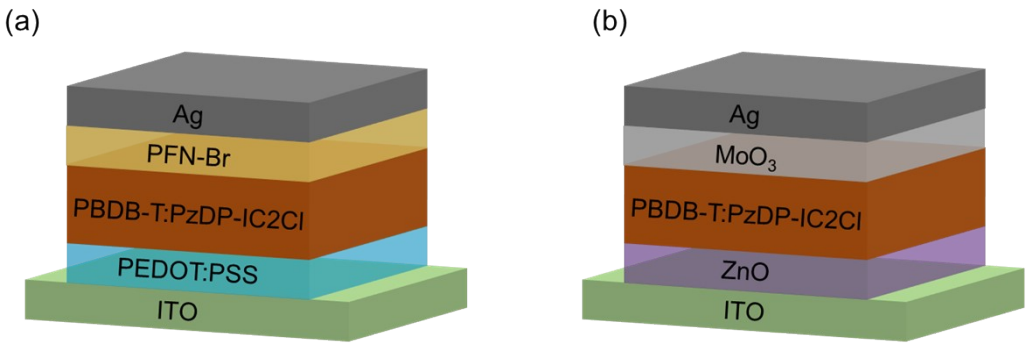

Fig. S22. Schematic diagrams of (a) conventional and (b) inverted devices.

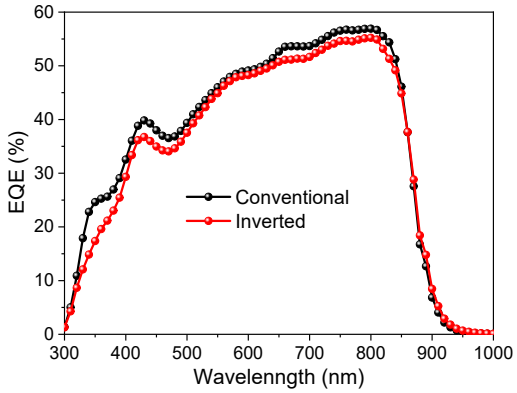

Fig. S23. EQE spectra of the OPDs based on PzDP-IC2Cl.

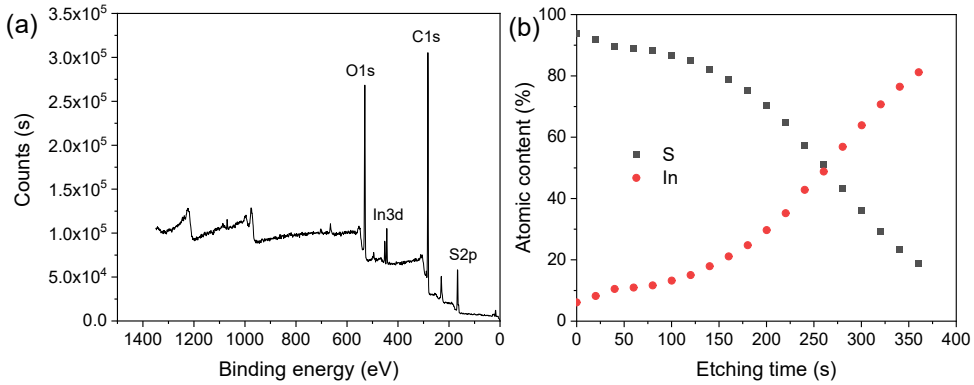

Fig. S24. (a) XPS survey spectrum at the surface of PEDOT:PSS layer (ITO/PEDOT:PSS), and (b) XPS depth profiles of PEDOT:PSS layer (ITO/PEDOT:PSS).

Notably, nitrogen and indium coexisted at the region close to the ITO substrate during the XPS depth profiling of the OPD devices (Fig. 3d). One possible reason for that is the reaction between the acidic PEDOT:PSS and ITO, leading to the release and concomitant diffusion of indium atoms[5-7] into the PEDOT:PSS layer or even further into the active layer. To support this supposition, we prepared a thin layer of PEDOT:PSS on top of an ITO substrate (ITO/PEDOT:PSS) with the same processing conditions as those in the fabrication of OPD device, and then conducted XPS analysis of this ITO/PEDOT:PSS sample. Sulfur and indium were adopted as the representative element for PEDOT:PSS and ITO respectively. At the surface of PEDOT:PSS layer, both sulfur and indium were detected as shown in Fig. S23a. As the etching progressed, the content of indium increased while that of sulfur decreased (Fig. S23b). The detection of indium at the surface of PEDOT:PSS layer is an convincing evidence for the coexistence of indium and nitrogen at the interface between the active layer and the PEDOT:PSS layer.

References

[1] W. Hong, B. Sun, C. Guo, J. Yuen, Y. Li, S. Lu, C. Huang, A. Facchetti, *Chem. Commun.* 2013, **49**, 484.

[2] G. Sivakumar, D. R. Bernardo, P. E. Marchezi, A. F. Nogueira, *Mater. Chem. Phys*. 2020, **240**, 122176.

[3] M. Sasikumar, D. Bharath, G. S. Kumar, N. R. Chereddy, S. Chithiravel, K. Krishnamoorthy, B. Shanigaram, K. Bhanuprakash, V. J. Rao, *Synth. Met.* 2016, **220**, 236

[4] M. J. Frisch, G. W. Trucks, H. B. Schlegel, G. E. Scuseria, M. A. Robb, J. R. Cheeseman, G. Scalmani, V. Barone,B. Mennucci, G. A. Petersson, H. Nakatsuji, M. Caricato, X. Li, H. P. Hratchian, A. F. Izmaylov, J. Bloino, G. Zheng, J. L. Sonnenberg, M. Hada, M. Ehara, K. Toyota, R. Fukuda, J. Hasegawa, M. Ishida, T. Nakajima, Y. Honda, O. Kitao, H. Nakai, T. Vreven, J. A. Montgomery, J. E. Peralta, F. Ogliaro, M. Bearpark, J. J. Heyd, E. Brothers, K. N. Kudin, V. N. Staroverov, R. Kobayashi, J. Normand, K. Raghavachari, A. Rendell, J. C. Burant, S. S. Iyengar, J. Tomasi, M. Cossi, N. Rega, J. M. Millam, M. Klene, J. E. Knox, J. B. Cross, V. Bakken, C. Adamo, J. Jaramillo, R. Gomperts, R. E. Stratmann, O. Yazyev, A. J. Austin, R. Cammi, C. Pomelli, J. W. Ochterski, R. L. Martin, K. Morokuma, V. G. Zakrzewski, G. A. Voth, P. Salvador, J. J. Dannenberg, S. Dapprich, A. D. Daniels, O. Farkas, J. B. Foresman, J. V. Ortiz, J. Cioslowski and D. J. Fox, *Gaussian-09*, *Revision A.02*, Wallingford CT.

[5] H.-K. Seo, H. Kim, J. Lee, M.-H. Park, S.-H. Jeong, Y.-H. Kim, S.-J. Kwon, T.-H. Han, S. Yoo, T.-W. Lee, Adv. Mater. 2017, 29, 1605587.

[6] H. Cho, Y.-H. Kim, C. Wolf, H.-D. Lee, and T.-W. Lee, Adv. Mater. 2018, 30, 1704587.

[7] H. Wang, H. Yuan, J. Yu, C. Zhang, K. Li, M. You, W. Li, J. Shao, J. Wei, X. Zhang, R. Chen, X. Yang, and W. Zhao, ACS Appl. Mater. Interfaces, 2020, 12, 53528.